Journal of Southeast University (English Edition) Vol. 41, No. 1, pp. 12-19 Mar. 2025 ISSN 1003-7985

Physical and numerical modeling of a framed anti-sliding structure for a mountainous railway line

QIU Ruizhe[1], LIU Kaiwen[1,2], YANG Zhixiang[3], MA Chiyuan[1], XIAO Jian[1], SU Qian[2]

(1. School of Civil Engineering, Southwest Jiaotong University, Chengdu 610031, China; 2. Key Laboratory of High-Speed Railway Engineering of Ministry of Education, Southwest Jiaotong University, Chengdu 610031, China; 3. Chengdu Branch of Sichuan Chengmian Cangba Expressway Co., Ltd., Chengdu 610213, China)

Abstract: To ensure the operational safety of railways in the landslide-prone areas of mountainous regions, a large-scale model test and numerical simulation were conducted to study the bending moment distribution, internal force distribution, deformation development, and crack propagation characteristics of a framed anti-sliding structure (FAS) under landslide thrust up to the point of failure. Results show that the maximum bending moment and its increase rate in the fore pile are greater than those in the rear pile, with the maximum bending moment of the fore pile approximately 1.1 times that of the rear pile. When the FAS fails, the displacement at the top of the fore pile is significantly greater, about 1.27 times that of the rear pile in the experiment. Major cracks develop at locations corresponding to the peak bending moments. Small transverse cracks initially appear on the upper surface at the intersection between the primary beam and rear pile and then spread to the side of the structure. At the failure stage, major cracks are observed at the pil-beam intersections and near the anchor points. Strengthening flexural stiffness at intersections where major cracks occur can improve the overall thrust-deformation coordination of the FAS, thereby maximizing its performance.

Key words: mountainous railway; slope; framed anti-sliding structure; model test; finite element modeling; mechanical responses

DOI: 10.3969/j.issn.1003-7985.2025.01.002

Landslides are among the most common and destructive geological hazards, causing significant loss of life and billions of dollars in damage annually[1-3]. To mitigate these hazards, anti-sliding piles are developed as an effective method[4-5] for transferring landslide thrust to more stable sublayers. Various types of anti-sliding structures are proposed to address different conditions, including combined piles, h-type anti-sliding piles[6], door-type piles, bent anti-sliding piles, and prestressed anchor piles.

To quantify the stabilizing effects of these structures, numerical approaches (e.g., limit analysis, finite difference method, and finite element method) are widely adopted by researchers to study the performance of various anti-sliding structures[7-13]. These studies highlight the effectiveness of numerical models in understanding the serviceability and ultimate limit states of these structures. Several experimental studies have also been conducted to evaluate the effectiveness of anti-sliding structures[14-16]. In the context of rapid urbanization in mountainous areas, a framed anti-sliding structure (FAS) is developed, enhancing the traditional h-type design by incorporating a secondary beam to improve stability and functionality, particularly for supporting infrastructure like railways. Previous studies have examined the responses of FASs during their operational period[17-18]. However, few studies have explored the stress-deformation evolution of FASs throughout their full lifecycle, from the elastic bearing stage to failure. Furthermore, the underlying failure mechanisms remain unclear. This gap in knowledge has resulted in overly conservative designs, hindering the full utilization of the capabilities of FASs and restricting their broad applications.

This study aims to investigate the performance of the FAS through physical tests and numerical simulations. A large-scale reduced-size experiment was conducted, deliberately bringing the structure to failure. The experimental setup, process, and results are discussed in detail. Following the physical test, a three-dimensional finite element simulation was performed to further explore the stress-deformation behavior throughout the FAS's entire lifecycle, as well as its failure mechanisms.

1 Engineering Background

Fig. 1 presents a typical cross-section of the DK53+200 segment of the Linzhi railway line in Guizhou Province, China, illustrating the application of the FAS on a slope. Originally, this slope was unstable, measuring approximately 860 m in length and 640 m in width, with

Received 2024-09-18, **Revised** 2024-11-28.

Biographies: Qiu Ruizhe (1995—), male, Ph. D. candidate; Liu Kaiwen (corresponding author), male, doctor, professor, kaiwenliu@swjtu.edu.cn.

Foundation item: The National Natural Science Foundation of China (No. 52078427).

Citation: QIU Ruizhe, LIU Kaiwen, YANG Zhixiang, et al. Physical and numerical modeling of a framed anti-sliding structure for a mountainous railway line[J]. Journal of Southeast University (English Edition), 2025, 41(1): 12-19. DOI: 10.3969/j.issn.1003-7985.2025.01.002.

a significant volume. Following several days of heavy rain, cracks began to form, significantly increasing the risk of a landslide, which would pose a serious threat to lives and property. To mitigate this risk, FASs were implemented as an anti-sliding structure and support for the transit pathway. After reinforcement, the slope had an incline of approximately 23°, with the soil thickness ranging from 5 to 15 m. Fig. 1 highlights an underlying weak soil layer that could potentially trigger landslides. To further stabilize the slope, a row of stabilizing piles was installed in the upper section, positioned 60 m away from the FAS.

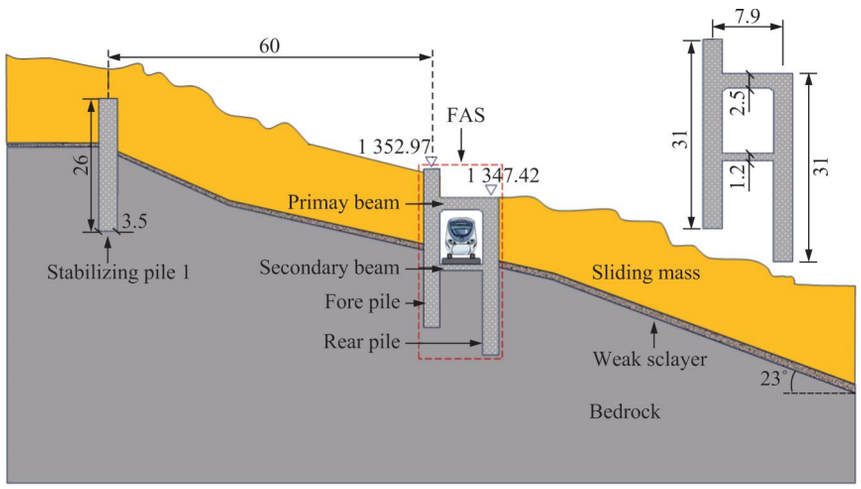

Fig. 1 Typical cross-section of DK53+200 in the Linzhi railway line (unit: m)

2 Experimental Tests

2.1 Scaling design

In this study, a scaled model test with a geometrical scaling factor λ of 20 was conducted to evaluate the responses of a prototype FAS applied to the slope. The Buckingham π theorem[19] was used to obtain the similarity relations for the experiments. Three independent ratios between the model and the prototype were maintained in the 1-g tests (i.e., the ratio of geometric size l is $1/\lambda$, the ratio of gravity acceleration g is 1, and the ratio of elastic modulus E is 1), and the conservation of the combinations π across the scales led to the similarity ratio for the rest of the parameters. All the related parameters and material properties are properly scaled and listed in Table 1.

Table 1 Dimension and similarity relation

Parameter	Similarity relation
Stress σ	1
Strain ε	1
Displacement u	$1/\lambda$
Flexural rigidity EI	$1/\lambda^4$
Inner friction angle φ	1
Moment M	$1/\lambda^3$
Reinforcement ratio ζ	1
Force F	$1/\lambda^2$

2.2 Test setup

2.2.1 Test facilities

As shown in Fig. 2(a), the testing system consists of three main components: the bedrock foundation, the resisting systems (i.e., FASs), and the thrust system.

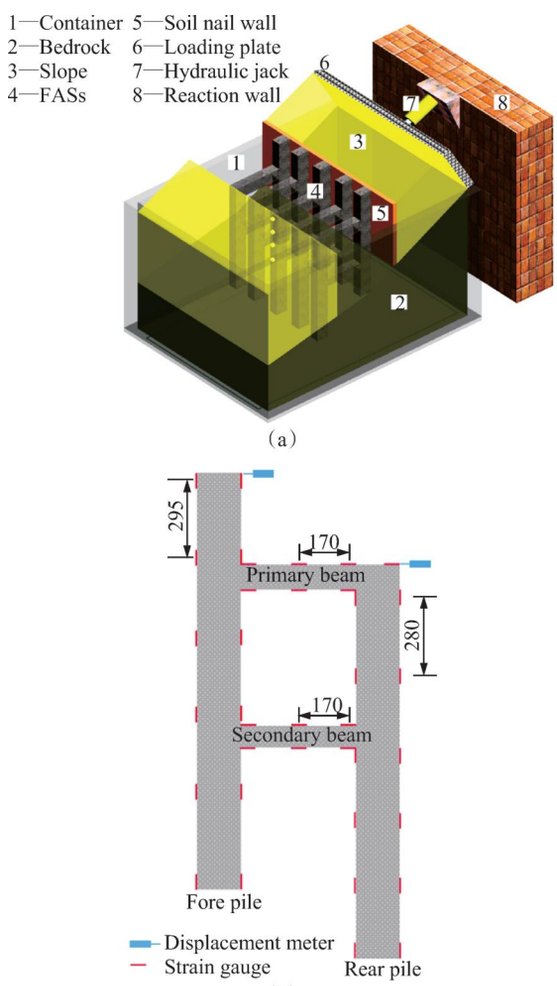

Fig. 2 Physical scale model. (a) 3D view of the model; (b) Arrangement of sensors on the FAS (unit: mm)

The computer-controlled thrust system comprises a hydraulic jack, pressure transducers, a reaction wall, and a steel plate that acts on the upper part of the soil. The FASs and the bedrock were situated inside a large steel container anchored to the ground. The container was 2 m in height, 3.5 m in length, and 2.0 m in width. The inner surface of the container was coated with a thin layer of lubricant to reduce the side friction between the soil and the inner wall. A total of five FASs, connected by the soil nail walls, were constructed to resist the upper part of the soil that was thrusted by the steel plate. The dimensions of the FAS model were calculated by the aforementioned similarity ratio and are provided in Table 2.

Table 2 Geometry size of scaled FASs in the model test

Parameter	Value
Dimension of fore piles/(mm×mm×mm)	100×150×1 550
Dimension of rear piles/(mm×mm×mm)	100×150×1 550
Dimension of primary beams/(mm×mm×mm)	125×100×395
Dimension of secondary beams/(mm×mm×mm)	60×50×395
Anchorage depth of fore piles/mm	750
Anchorage depth of rear piles/mm	750

Only the FAS located in the middle of the system was monitored to avoid the boundary effects. The arrangement of the strain gauges (BMB120-3AA(11)-P3000-D) and displacement meters (V-DCD50-S1-B-7-L1) are displayed in Fig. 2(b). A total of 12 strain gauges were placed on the front and back surfaces of the rear pile with a spacing of 280 mm, and a total of 12 strain gauges were implemented on the front and back surfaces of the fore pile with a spacing of 295 mm. The strain gauges on the primary and secondary beams were spaced 170 mm apart. Two displacement meters were placed on the top of the fore and rear piles to measure displacement. In addition, a camera was used to monitor the damage to the FASs and the slope surface during the application of thrust.

2.2.2 Model materials

The prototype steel bars and aggregates for C40 concrete could not be uniformly poured into the mold of the scaled FASs. As a result, self-made reinforced concrete with fine aggregates was used, with an aggregate size of less than 5 mm and steel bars (tensile strength of 360 MPa) with a diameter of 6 mm. After adjusting the mix ratios, it was determined that self-made reinforced concrete with a water-to-cement ratio of 0.48 and an aggregate-to-cement ratio of 3 could replicate the properties of C40 concrete. For the scaled soil nail wall, a 15 mm wooden board with equivalent bending stiffness was used as a substitute. C20 plain concrete was applied for the bedrock material to ensure sufficient rigidity and strength to anchor the FASs. The slope was modeled using gravel soil sourced from the project site, with a compaction degree of 90%.

2.3 Test procedure

The reinforcement skeleton, as shown in Fig. 3(a), was first fabricated and placed into the mold. Self-made concrete was then poured into the mold in two batches to form the FASs. The mold's inner surface was coated with a thin layer of Vaseline to facilitate the demolding process. After curing, 16 pairs of strain gauges were symmetrically attached on either side of piles and beams according to the spatial arrangement described earlier (Fig. 3(b)). Before pouring concrete to construct the bedrock, polyvinyl chloride pipes were installed at the location of the fore and rear piles of the FASs to provide wiring space for the monitoring system, including various sensors (Fig. 4(a)). Once the bedrock had solidi-

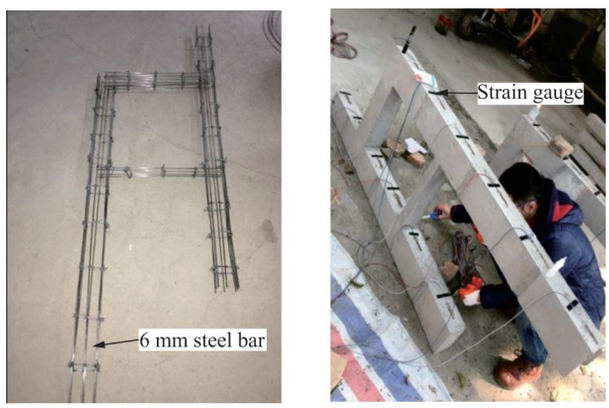

Fig. 3 Preparation of FASs. (a) Steel skeleton; (b) Layout sensors

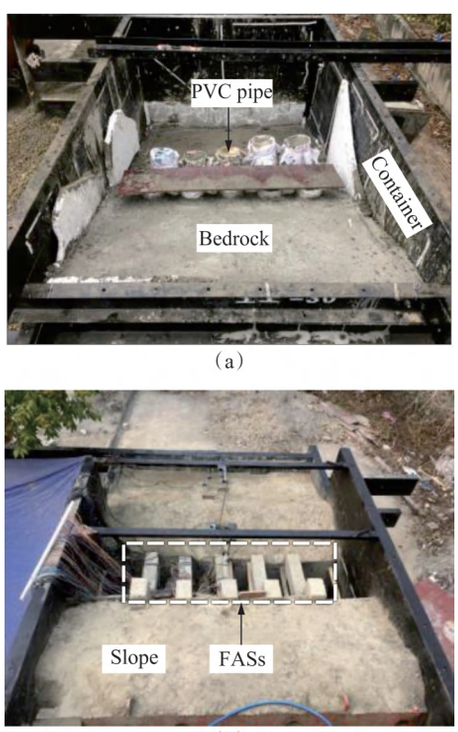

Fig. 4 Construction of the physical scale model. (a) Reserve space for FAS and pour the bedrock; (b) Install FASs and fill the slope

fied, gravel soil was filled and compacted inside the container until the required degree of compaction was achieved (Fig. 4(b)). Finally, incremental thrust was applied using a hydraulic jack, and the responses of the FASs were closely monitored. Each incremental thrust was 20 kN, with constant pressure maintained for 15 min before adding the next increment. The test procedure stopped when significant slippage occurred at the slope-bedrock interface or when pile damage was observed.

3 Three-Dimensional Finite Element Model

In this section, a three-dimensional finite element model based on the experiment was developed using ABAQUS software, and comparisons were made with the data directly measured from the experiment. The geometric dimensions of the numerical model match those of the physical model test, as shown in Fig. 5(a). The model of the simulation consists of four key components: FASs, soil nail wall, slope, and bedrock. The bedrock and the soil nail wall were considered linear elastic material. The slope was modeled as a linearly elastic, perfectly plastic material with the Mohr-Coulomb criterion. The friction angle and cohesion for the slope were determined based on a consolidation drainage triaxial compression test. The Poisson's ratio of 0.18 and the elastic modulus of 20 MPa were assigned to the slope. The FASs were modeled as an isotropic elastoplastic concrete, using Mohr-Coulomb material with a cohesion of 3.34 MPa and a friction angle of 51.5°, as recommended by Cong et al. [20]. All detailed parameters used in the finite element model are provided in Table 3. The tie constraint was adopted for the interface between the FASs and bedrock as well as the FASs and soil nail wall. For the bedrock-slope interface, a surface-to-surface contact was applied with hard contact in the normal direction and a tangential friction coefficient of 0.7. For the soil nail wall-slope interface, a surface-to-surface contact was also applied, with hard contact in the normal direction and a tangential friction coefficient of 0.36. The bottom of the model was fixed in all three directions, with the sides of the model constrained in the X and Y directions. Finite element simulation consisted of two steps. First, the gravity load ($1g$) and geostatic stress were applied to achieve the *in situ* stress state. In the second step, thrust was applied perpendicular to the loading surface, starting with an initial thrust of 20 kN and increasing incrementally by 20 kN until a maximum of 180 kN was reached. Throughout both steps, the gravity load was applied using the predefined field manager in ABAQUS.

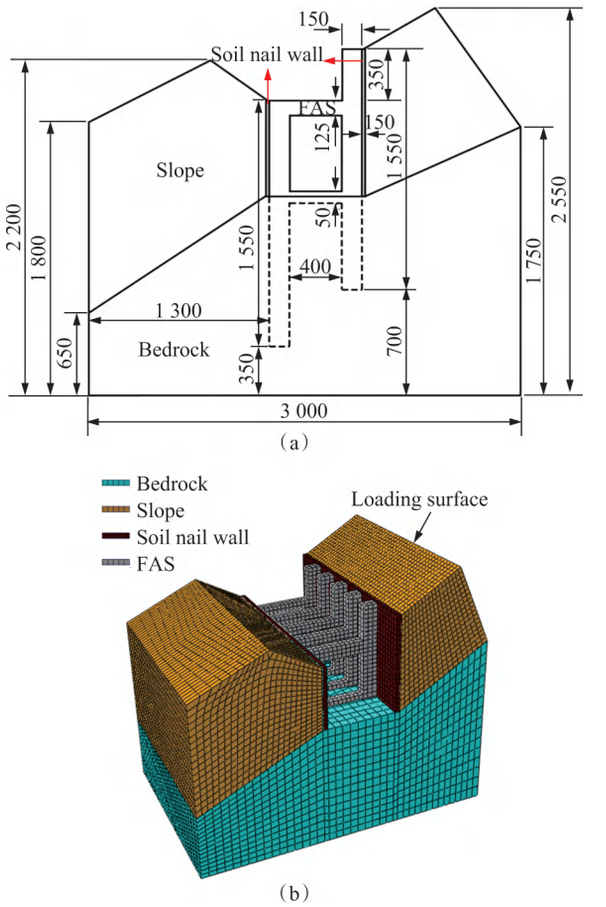

Fig. 5 Finite element model for physical model. (a) Dimension of the finite element model (unit: mm); (b) Finite element mesh

Table 3 Material parameters in the finite element model

Material	Young's modulus/MPa	Poisson's ratio	Unit weight/(kN·m^{-3})	Cohesion/kPa	Friction angle/(°)
Slope	20	0.18	20	15	25
FAS	32 500	0.20	24	3 340	51.5
Soil nail wall	11 000	0.25	8		
Bedrock	26 000	0.27	24		

4 Results and Discussion

4.1 Bending moment

The bending moment M can be calculated from one set of recorded strains on both sides of the piles or beams at the same cross-section by Eq. (1).

$$M = \frac{EI(\varepsilon_t - \varepsilon_c)}{l_d} \tag{1}$$

where ε_t and ε_c are the tensile (positive) and compressive (negative) strains of the same cross-section, respectively; l_d is the distance of one set of strain gauges.

The bending moment profiles of the fore and rear piles are shown in Fig. 6, with the experimental and numerical

results displaying strong agreement. As illustrated in Fig. 6(a), the bending moment of the fore pile forms a rotated W shape, increasing linearly as the applied thrust increases. The maximum bending moment occurs at the anchor points. When the applied thrust is 60 kN, the maximum bending moment is approximately 780 N·m, and for every additional 40-kN thrust, the maximum bending moment increases by about 700 N·m. In Fig. 6(b), the bending moment of the rear pile exhibits an inverted V shape, also increasing linearly with the applied thrust. The maximum bending moment of the fore pile is approximately 1.1 times that of the rear pile. For every 40 kN increase in thrust, the maximum bending moment of the rear pile increases by approximately 650 N·m. Therefore, a larger bending moment is observed in the fore pile, suggesting that it should be designed to be stronger than the rear pile.

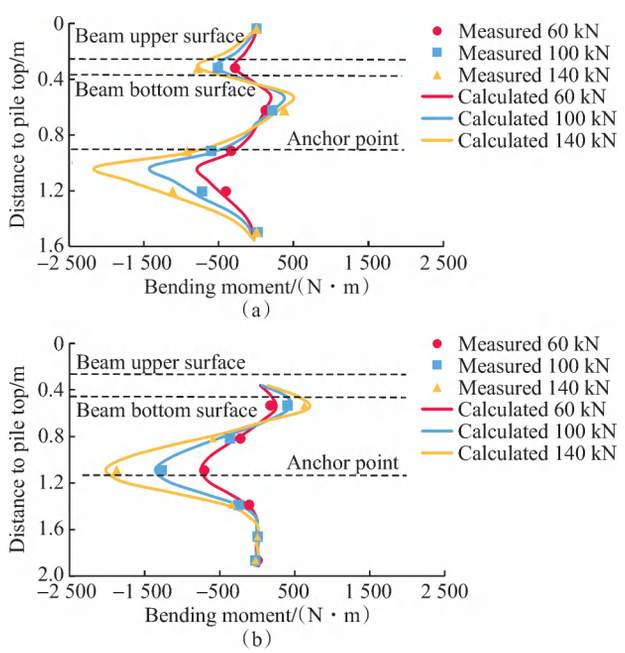

Fig. 6 Distribution of the bending moment along piles. (a) Fore pile; (b) Rear pile

Fig. 7 shows the distribution of the bending moment along the primary and secondary beams. Within the range of 0 to 0.23 m, the bending moment in both beams decreases as the distance to the pile increases. Beyond 0.23 m, the bending moment gradually increases with the distance to the fore pile. Since the bending moment in the fore pile is larger than that in the rear pile, the zero points of the bending moments in both the primary and secondary beams are positioned closer to the rear pile. The distance ratio of these zero points to the fore and rear piles is approximately 5∶3. Overall, the bending moment in the primary beam is greater than that in the secondary beam.

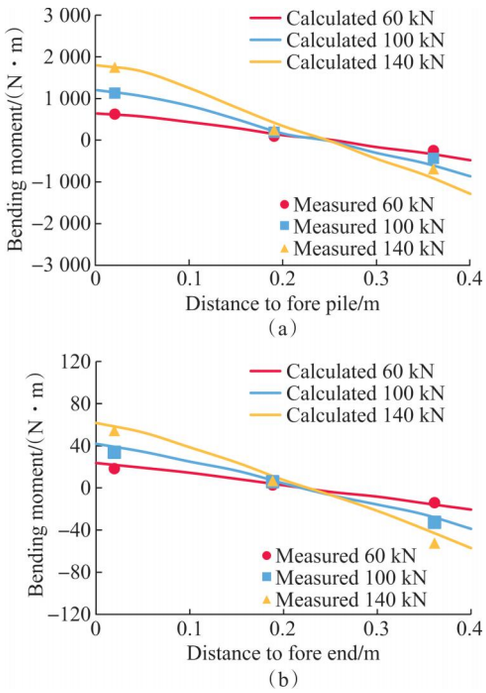

Fig. 7 Distribution of the bending moment along the beams. (a) Primary beam; (b) Secondary beam

4.2 Displacement

Fig. 8 illustrates the variation in the displacement at the top of the fore and rear piles as the thrust gradually increases. The experimental and numerical results demonstrate that the displacement at the top of the fore and rear piles increases with the applied thrust. Numerical simulations align closely with the experimental data when the

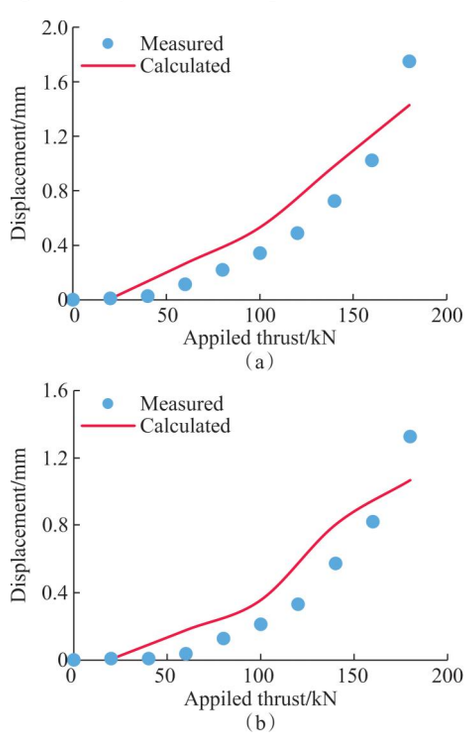

Fig. 8 Development of displacements at the top of piles. (a) Fore pile; (b) Rear pile

thrust is below 160 kN, although the numerical results are slightly higher. However, when the thrust increases from 160 to 180 kN, the displacement increment in the experiment is significantly larger than that in the numerical simulation. This is due to the unstable development of cracks in the experiment during the thrust stage, leading to failure. Additionally, the displacement at the top of the fore pile is consistently greater than that of the rear pile as the thrust increases. At a thrust of 140 kN, the displacement at the top of the fore pile is 1.27 times greater than that of the rear pile and 1.22 times greater in the numerical simulation. This indicates a higher degree of deformation in the fore pile when subjected to thrust from the slope.

4.3 Locations of cracking

This section analyzes crack formation to identify vulnerable locations in the FAS. The appearance and progression of cracks as the thrust increases can be categorized into three stages: elastic stage (0 to 100 kN), crack development stage (100 to 160 kN), and steel bar yield stage (greater than 160 kN). During the first stage, no cracks were observed on the FASs, with the largest stress concentrated on the lower surface of the FASs at the intersection between the secondary beam and fore pile (Fig. 9(a)). In the second stage, the largest stress shifted to the upper surface at the intersection between the primary beam and the rear pile. The stress at this position exceeded the ultimate tensile stress of C40 concrete, leading to the formation of transverse cracks at the same position (Fig. 9(b)). With further thrust application, the region where tensile stress surpassed the ultimate tensile stress of C40 concrete expanded. Specifically, at the intersection between the primary beam and rear pile, the region experiencing critical stress grew from the upper surface of the intersection to the sides, which corresponded with the lateral spread of transverse cracks along the FAS structure (Fig. 9(c)). In the third stage, when thrust surpassed 160 kN, the region experiencing critical stress extended across the entire cross-section of the intersection between the primary beam and rear pile, resulting in the formation of a plastic hinge at this location (Fig. 9(d)). As stress of the steel bars gradually exceeded their yield strength, the structure's bearing capacity dropped sharply, leading to failure. Post-failure observations revealed major cracks at the intersections between the piles and beams as well as near the anchor points. These locations align with the peak values observed in the bending moment diagrams (Figs. 6 and 7). Although bending moments at the anchor points of the fore and rear piles were larger than those experienced by the beams, cracks were first developed in the primary beam because of its lower flexural stiffness. This finding suggests that, in this engineering, enhancing the flexural stiffness of the primary beam could improve the overall thrust-deformation coordination of the FAS, thereby increasing its structural resilience.

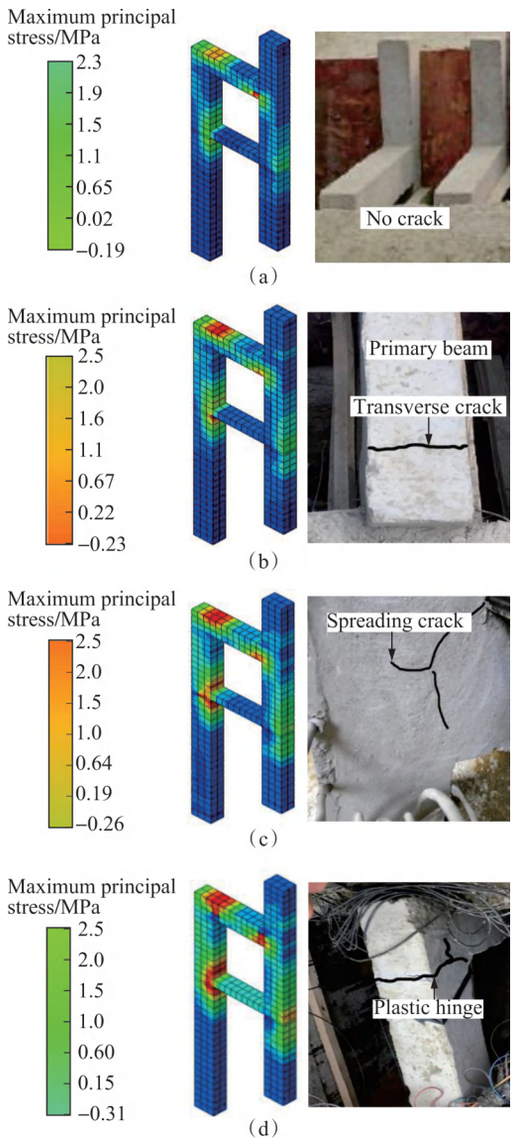

Fig. 9 Variation in stress with slide thrust. (a) 60 kN; (b) 100 kN; (c) 140 kN; (d) 180 kN

5 Limitations and Discussion

Meeting all similarity criteria precisely is unfeasible. In this study, a jack was used to apply thrust to the FAS until failure, making the effects of a unit weight (i.e., density) on the FAS responses a secondary factor. Thus, the exact similarity in the unit weight (i.e., density) is less crucial. The bedrock serves as an anchor for the FAS, while the soil nail wall connects the structure and transfers thrust. Therefore, provided that the bedrock and soil nail wall have adequate strength to prevent failure, strict material similarity can be relaxed.

This paper focuses on the FAS performance for a slope under landslide thrust, excluding train loads from the current analysis. Future studies will incorporate train loads, focusing on the dynamic response of the FASs.

6 Conclusions

This paper investigated the performance of a newly developed FAS through physical model tests and numerical simulation. The scaled physical model was tested under simulated landslide thrust until failure. A corresponding finite element simulation was developed to replicate the experimental results, which showed good agreement with the test data, enhancing the understanding of the stress distribution and failure mechanisms. Based on the results and discussions, the following conclusions can be drawn.

(1) The maximum bending moments in both piles occurred at the anchor points and increased linearly with the applied thrust. The fore pile experienced higher stress concentrations than the rear pile.

(2) Under slope thrust, the fore pile exhibited more deformation compared to the rear pile. At a thrust of 140 kN, the displacement at the top of the fore pile was 1. 27 times greater than that of the rear pile in the experiment and 1. 22 times greater in the numerical simulation.

(3) As the thrust increased, the small transverse cracks were first appearance at the intersection between the primary beam and the fore pile. With further thrust increase, the cracks expanded to the sides of the FAS. Finally, concrete at the intersection between the primary beam and piles exceeded its ultimate tensile stress, forming a plastic hinge and leading to the failure of the FASs.

References

[1] HE H J, LAN J W, CHEN Y M, et al. Monitoring and stability analysis of slope slip of a landfill with multiple intermediate covering layers [J]. Journal of Southeast University (English Edition), 2018, 34(1): 104-111.

[2] XIONG W, WAN Y H, HOU X T, et al. Fundamental experiments on landslide prediction based on acoustic emission monitoring[J]. Journal of Southeast University (Natural Science Edition), 2016, 46(1): 184-190. (in Chinese)

[3] ZHAN C H, YANG Z Y, WU W B. Experimental study on the permeability of ecological slopes under rainfall infiltration conditions [J]. Applied Sciences, 2023, 13 (17): 9610.

[4] POULOS H G. Design of reinforcing piles to increase slope stability [J]. Canadian Geotechnical Journal, 1995, 32(5): 808-818.

[5] LI Z, LIU T, LIU L L, et al. Stability evaluation of supported high and steep loess slope based on D-S evidential reasoning[J]. Journal of Southeast University (Natural Science Edition),2023,53(3):436-444. (in Chinese)

[6] ZHAO B, WANG Y S, WANG Y, et al. Retaining mechanism and structural characteristics of h type anti-slide pile (hTP pile) and experience with its engineering application [J]. Engineering Geology, 2017, 222: 29-37.

[7] WEI W B, CHENG Y M. Strength reduction analysis for slope reinforced with one row of piles[J]. Computers and Geotechnics, 2009, 36(7): 1176-1185.

[8] LIU K W, SHAO K, EL NAGGAR M H, et al. Dynamic performance of a railway subgrade reinforced by battered grouted helical piles[J]. Journal of Geotechnical and Geoenvironmental Engineering, 2024, 150(10): 05024009.

[9] LI L C, LIU X, LIU H, et al. Experimental and numerical study on the static lateral performance of monopile and hybrid pile foundation [J]. Ocean Engineering, 2022, 255: 111461.

[10] ZHANG J, WANG H, HUANG H W, et al. System reliability analysis of soil slopes stabilized with piles[J]. Engineering Geology, 2017, 229: 45-52.

[11] ZHANG H K, LI C D, YAO W M, et al. A novel approach for determining pile spacing considering interactions among multilayered sliding masses in colluvial landslides[J]. KSCE Journal of Civil Engineering, 2019, 23 (9): 3935-3950.

[12] ZHANG P Y, XIONG L C, LE C H, et al. Comparison analysis of the bearing capacity of rock-socketed piles and sand piles for offshore wind turbines[J]. Journal of Southeast University (English Edition), 2023, 39(4): 384-392.

[13] CAI Y S, ZHENG J F. Stability analysis of Huangtupo sliding land at badong town in Yangzhi river three gorges and the prevent sliding measure[J]. Journal of Southeast University (Natural Science Edition), 2001, 31 (5): 53-57. (in Chinese)

[14] LI C D, WU J J, TANG H M, et al. Model testing of the response of stabilizing piles in landslides with upper hard and lower weak bedrock[J]. Engineering Geology, 2016, 204: 65-76.

[15] LIU X R, KOU M M, FENG H, et al. Experimental and numerical studies on the deformation response and retaining mechanism of h-type anti-sliding piles in clay landslide[J]. Environmental Earth Sciences, 2018, 77 (5): 163.

[16] HU X L, ZHOU C, XU C, et al. Model tests of the response of landslide-stabilizing piles to piles with different stiffness[J]. Landslides, 2019, 16(11): 2187-2200.

[17] CHEN Z W, LI A H, HU H X, et al. Engineering technology of framed anti-slide retaining structure crossing ancient landslide[J]. Chinese Journal of Rock Mechanics and Engineering, 2021, 40(S1): 2861-2875. (in Chinese)

[18] GUO C M, SU Q, LIU J, et al. Study on mechanical characteristics and key design parameters of frame type anti-slide retaining structure[J]. Subgrade Engineering, 2019, (6): 13-17. (in Chinese)

[19] BUCKINGHAM E. On physically similar systems: Illustrations of the use of dimensional equations[J]. Physical Review, 1914, 4(4): 345-376.

[20] CONG Y, KONG L, ZHENG Y R, et al. Experimental study on shear strength of concrete[J]. Concrete, 2015, 5: 40-45.

山区铁路框架式抗滑结构模型试验及数值模拟

邱睿哲[1], 刘凯文[1,2], 杨智翔[3], 马驰原[1], 肖健[1], 苏谦[2]

(1.西南交通大学土木工程学院,成都 610031;2.西南交通大学高速铁路线路工程教育部重点实验室,成都 610031;
3.四川成绵苍巴高速公路有限责任公司成都分公司,成都 610213)

摘要: 为保证山区滑坡易发地区铁路的运营安全,通过大比例尺模型试验和数值模拟方法研究了山区铁路框架式抗滑结构在滑坡推力作用下直至结构失效过程中的弯矩分布特点、内力分布特点、变形发展规律及裂缝发展规律。结果表明,前桩的最大弯矩及增加率均大于后桩,前桩的最大弯矩约为后桩的1.1倍。当框架式抗滑结构失效时,前桩桩顶位移更为显著,大约是后桩的1.27倍。主要裂缝出现在与峰值弯矩对应的位置。横向微小裂缝首先出现在主梁与后桩连接处的上表面,随后扩散至结构侧面。在失效阶段,主要裂缝出现在桩-梁交接处及锚固点附近。增强主要裂缝发生截面的抗弯刚度,可以提高框架式抗滑结构的整体荷载-变形协调性,从而最大限度地发挥结构的性能。

关键词: 山区铁路;边坡;框架式抗滑结构;模型试验;有限元模拟;力学响应

中图分类号: U416.1